


Analysis of the Effects of a Rotating Rock on Rockfall Protection Barriers

Xin Qi  · Xiangjun Pei · Rui Han · Yafeng Yang · Qingcheng Meng · Zhixiang Yu

Received: 7 November 2017 / Accepted: 24 March 2018 / Published online: 31 March 2018
© Springer International Publishing AG, part of Springer Nature 2018

Abstract Due to limitations associated with field tests and equipment, the majority of the research conducted to evaluate the mechanical behaviour of rockfall protection barriers considers only free-falling rocks when simulating the actual situation. Based on this fact, this study introduces ψ , the ratio of the rotational kinetic energy to the kinetic energy of a rockfall, to study the rotational effect and to achieve an optimal design. LS-DYNA is used to analyse the dynamic response of the system under the impact of a rolling rock. The results indicate that a rolling rock is an adverse condition. As ψ increases, the rock displacement decreases with a clear outward rolling, which causes greater deformation of the energy dissipater of the upper support rope and greater displacement of the free end of the steel post. As ψ approaches 0.2, the tensile forces of the upper support rope and the anchor rope reach their peak values, which are 39% higher than the corresponding values

when ψ is 0. Additionally, the maximum forces of the steel post and net increase by 29 and 20%, respectively. The energy consumption of the break rings and wire ring net decrease linearly. However, the slide energy and friction energy increase linearly. To facilitate further research, correction coefficients that incorporate the effect of a rotational impact and formulas that include a relation between ψ and the force of each component are obtained through curve fitting.

Keywords Rockfall protection barrier · Full-scale test · Numerical simulation · Rotational kinetic energy · Dynamic response

List of symbols

V	Translational speed of the rockfall
V_0	Total speed of the rockfall
H	Height of the rockfall
g	Gravitational acceleration
α	Slope angle
k	Resistance coefficient of the rockfall along the hillside
E_a	Total energy of the rockfall
E_{va}	Translational kinetic energy
E_{ra}	Rotational kinetic energy
J	Moment of inertia
ω	Angular velocity of the rockfall
ψ	Ratio of the rotational kinetic energy to the translational kinetic energy

X. Qi (✉) · R. Han · Y. Yang · Z. Yu
School of Civil Engineering, Southwest Jiaotong
University, Chengdu 610031, China
e-mail: qixin_117@126.com

X. Qi · X. Pei
State Key Laboratory of Geohazard Prevention and
Geoenvironment Protection, Chengdu University of
Technology, Chengdu 610059, China

Q. Meng
School of Civil Engineering and Architecture, Southwest
Petroleum University, Chengdu 610500, China

H_f	Horizontal distance between the anchorage point of the anchor rope and the block centroid
H_v	Vertical distance between the lower surface of the block and the lowest end of the support rope
H_{max}	Maximum block displacement
F_{max}	Maximum internal force of each component
σ_{max}	Maximum internal stress of the steel post
η	Correction factor that considers the rotation effect

1 Introduction

A collapse that results in a rockfall due to topography, natural weathering, earthquakes, human activities, and other factors often poses a serious risk to traffic safety for railways and roads along mountain slopes. In recent years, frequent earthquakes and unstable rocks have increased the risks that rockfalls cause to not only traffic but also earthquake disaster relief, in which blockage of a vital lifeline constitutes a significant obstacle for a rescue. Rockfall protection barriers are highly impact resistant and have flexible layouts. The design of these barriers incorporates factors such as the type of mountain collapse and debris flow as well as other disaster prevention and control techniques. The rockfall protection barrier comprises four main parts: steel wire ring net, fixed system (anchor rope, base and support rope), break rings and steel posts. The system intercepts a collapsing rockfall mainly by net deformation, steel post hem, and break ring deformation. The components of the system are shown in Fig. 1.

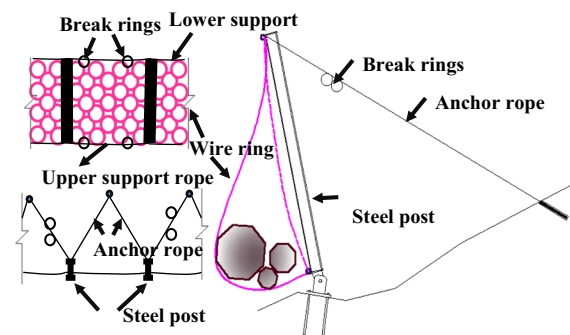


Fig. 1 Components of rockfall protection barrier

When the rockfall impacts the barrier, the wire ring net changes from a relaxed state to a tensile state, and the force is transferred to the upper and lower support ropes. Then, due to the force applied to the steel posts, the steel posts rotate in the plane, and the anchor ropes are pulled tight. When the force reaches a certain limit, the break rings start to deform, which consumes energy. Scholars have performed full-scale tests to study the mechanical characteristics and failure mode of these barriers. Suits et al. (2009) studied the performance of nets under different stress conditions. Gottardi and Govoni (2010) studied the mechanical properties of barriers by experimenting with different levels of rock freefall impacts. Buzzi et al. (2013) studied the rock-to-pendulum movement impact of four groups of low-level barriers and rock freefall impact net tests with a comparative analysis of the low-level barrier work performance. Several scholars have conducted numerical simulations of the entire barrier and analysed the key parameters. Gentilini et al. (2012, 2013) established an ABAQUS/explicit numerical model by using three groups of freefall impact full-scale barrier test data with a numerical simulation to verify the accuracy of the comparison. Comparisons in many experiments and numerical simulations show that the finite element method is an effective means of analysis and achieves good results. Moon et al. (2014) established an overall model of the barrier; the effects of the angle between the steel post and the ground, the angle of entry of the rockfall, the spacing of the steel post and the energy dissipation on the capacity of the barrier were studied through parametric adjustments. Koo et al. (2017) established an overall model of different force conditions of single-rock and multi-rock falls for different vertical and horizontal impacts and studied the effect of the rock impact area on the barrier. Several scholars have compared simulation models with experimental tests.

In the event of earthquakes, landslides and other disasters, the rockfall on a slope, which includes rolling, sliding, and impact rebound (Spadari et al. 2013), is the main form of movement. Currently, experimental studies on rockfall protection barriers are limited by the initial velocity of existing test sites. A majority of the impacts are simulated as uniaxial impacts, which does not account for complex conditions, such as flying and rolling rocks. Because the rotational effect of the rock is neglected, the test results are different from the field. Although a

supplementary note of Technical Approval of Falling Rock Protection Kits (ETAG 27) (EOTA 2012) mentions that rockfall rolling should be considered, there is no specific numerical value or calculation method. Therefore, the Transportation Research Board of the National Academies (National Council 2009) and the Swiss Agency for the Environment, Forests and Landscape (Glover et al. 2010) have conducted full-scale impact tests on a rockfall attenuator and hybrid drape system. They discussed the rolling effect of rockfall on the damage characteristics of a metal net, but the focus was not the entire rockfall barrier system. Few studies consider the effect of rock rotation, so the actual situation is quite different from the results. Therefore, the effect of rockfall rotation on the barriers must be investigated.

2 Initial Motion State of a Rockfall

The rock trajectory and distribution are simplified to only consider the rock and barrier contact moments. The initial state of the rockfall can be divided into three stages: rotating, sliding and straight down motions (Volkwein 2005). In this paper, a rotating model that ignores the frictional resistance is the base model. In the falling process, the rock converts gravitational potential energy into translational and rotational kinetic energies.

According to Fig. 2, the rockfall speed can be calculated using formulas (1) and (2) (Hu 1989).

$$V = u\sqrt{2gH} = uV_0 \tag{1}$$

$$u = \sqrt{1 - kctg\alpha} \tag{2}$$

where V is the translational speed of the rockfall, V_0 is the total speed of the rockfall, H is the height of the rockfall, g is the gravitational acceleration, α is the

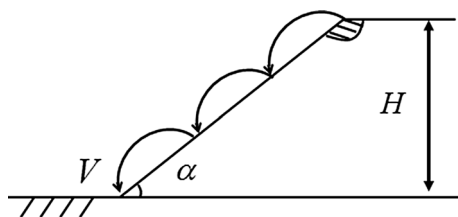


Fig. 2 Rockfall along a hillside fall

slope angle, and k is the resistance coefficient of the rock along the hillside, which is affected by all relevant factors.

The total energy of the rockfall is E_a . The E_{va} is the translational kinetic energy and E_{ra} is the rotational kinetic energy. Assume that the energy loss of the rockfall is entirely converted into kinetic energy. The parameter ψ is defined as the ratio of the rotational kinetic energy to the translational kinetic energy (E_{ra}/E_{va}); therefore, formula (7) can be derived.

$$E_a = \frac{1}{2}mV_0^2 \tag{3}$$

$$E_{va} = \frac{1}{2}mV^2 \tag{4}$$

$$E_{ra} = E_a - E_{va} = \frac{1}{2}J\omega^2 \tag{5}$$

$$\frac{E_{ra}}{E_{va}} = \psi \tag{6}$$

$$\psi = \frac{1 - \mu^2}{\mu^2} \tag{7}$$

where J is the moment of inertia and ω is the angular velocity of the rockfall.

According to existing research, the interception capacity of flexible protective barriers ranges from 200 to 5000 kJ. Currently, the interception capacities of the most common models of flexible intercepting barrier are 500, 1000, 1500 and 2000 kJ. The research shows that although different types of the barrier exist, the energy distribution, internal forces and working characteristics of the system are basically the same. Therefore, in this paper, we selected a protective barrier with the interception capacity of 1000 kJ as the research object and performed the corresponding experiment and numerical simulation.

3 Full-Scale Test

The rockfall impact test shown in Fig. 3 refers to the representative standard ETAG 27. The test site, located in Xinjin County (Sichuan, China) includes a reaction wall, a cantilever crane and testing equipment. The test model has three functional modules and four steel posts with a height of 5 m. The horizontal spacing between the posts is 10 m. The post feet are

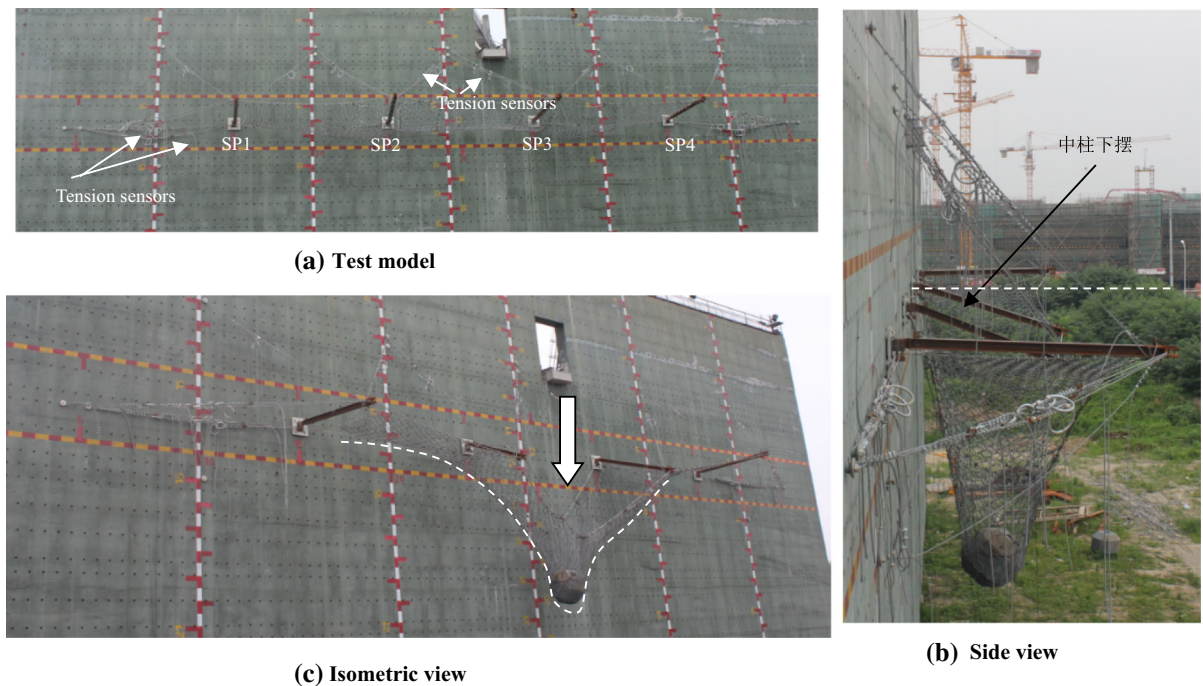


Fig. 3 Full scale test. **a** Test model, **b** side view and **c** isometric view

fixed on the RC reaction wall by a pin hinge that provides rotational freedom in the vertical plane, and the post caps are connected to the uphill rope. All of the posts and the net are set horizontally and are subjected to the impact load of a free-falling block. Tension sensors are set in the ends of the support ropes and anchor ropes to monitor the tension history. A 6170 kg test block is raised 17 m, and the test block free fall impact centre position is the middle of the span. The full-scale test model and test results are shown in Fig. 3.

4 Numerical Simulation of the Rockfall Barrier

4.1 Finite Element Model

A finite element analysis of the contact collision between a barrier and rockfall involves a complex problem of geometric nonlinearity, material nonlinearity and boundary condition nonlinearity. The explicit analysis method of conditional stability has notable advantages in considering this type of problem. When the mass matrix is diagonalized, there is no need to establish and solve simultaneous equations,

which reduces the memory requirements and increases the calculation speed. The following analyses are based on the LS-DYNA explicit algorithm.

The rock element is simulated by a solid element, the net is a three-node second-order beam element, and the rope is a cable. The sliding element simulates the sliding of the rope along the steel post saddle, the three-stage nonlinear spring simulates the break ring, and the space beam element simulates the steel post. The rock and rope use a contact boundary. The bottom of the steel post in the vertical plane can be regarded as an ideal articulation. Out-of-plane constraints can be regarded as the bending spring of the limited free rotation (Zhao et al. 2013). The basic structure of the barrier is shown in Fig. 4, and the material characteristics of the main components are given in Table 1.

5 Comparison Between the Test and Numerical Simulation Results

To verify the numerical model, the numerical simulation results and the test results are compared. The displacements of key points are in agreement between the two sets of results (Table 2). The numerical

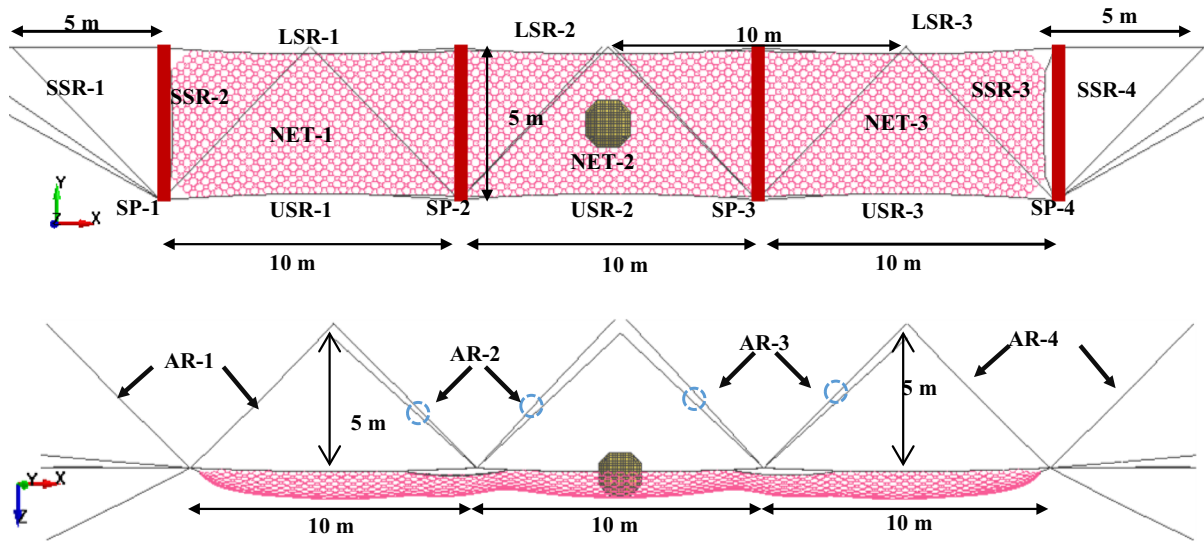


Fig. 4 Finite element model

Table 1 Material properties

	Density (kg/m ³)	Elastic modulus (GPa)	Poisson's ratio	Yield stress (MPa)
Block	2515	20	0.3	–
Break ring	7900	150	0.3	–
Wire ring net	7900	150	0.3	1770
Steel post	7900	200	0.3	235
Rope	7900	150	–	–

Table 2 Displacement of key points

	Simulation (m)	Test (m)	Deviation (%)
Max displacement	6.28	5.9	6
<i>Vertical displacement</i>			
SP-1	0.3	0.3	0
SP-2	0.6	0.8	33
SP-3	0.6	0.5	16
SP-4	0.3	0.4	33

simulation results are slightly larger than the experimental results because the numerical simulation results select the maximum value during the impact process, while the test results are the values after the block stabilized because the wire-ring net still has some elasticity because it does not fully enter the plastic stage. Therefore, when the impact reaches the maximum displacement value, the block rebounds, which results in a smaller value after stabilization. The impact of the test process has a certain deviation that is not the centred around the midspan, which results in

asymmetric test results. The numerical simulation can strictly control the impact position, so the results are symmetrical. As a result, the vertical displacements of the two ends posts are very different.

The tension history of the ropes in the test is in good agreement with the numerical analysis. The order of the peak tensile forces of the ropes is as follows: lower support rope, upper support rope, and anchor rope, which is consistent with the force transmission path of the system (Fig. 5).

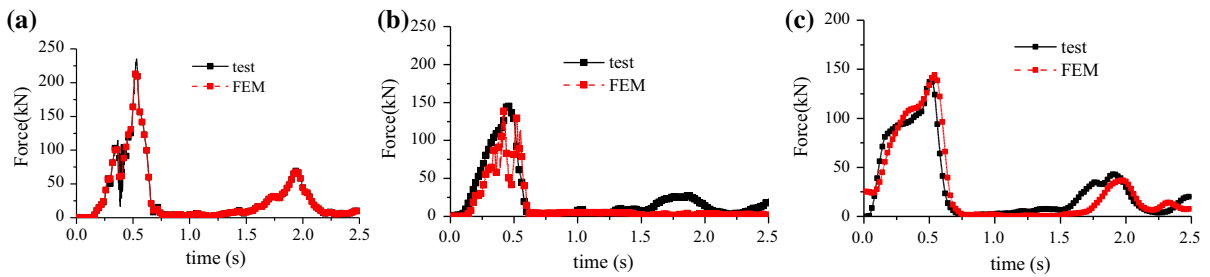


Fig. 5 Comparison of the tension history: **a** lower support rope, **b** upper support rope, and **c** anchor rope

6 Calculation Condition

To facilitate the calculation, different ψ value from 0 to 0.4 are used. According to formula (7), the hillside slope angle is $79^\circ\text{--}90^\circ$, which covers the most unfavourable slope angles that are prone to danger, as shown in Table 3. The rotational kinetic energy of the rockfall (corresponding to different ψ) and the translational kinetic energy are shown in Table 4.

Based on the same barrier model, a total of five conditions are established, in which each condition satisfies $E_{va} + E_{ra} = 1000$ kJ. When the vertical initial velocity is applied, the block rotates around its centre of mass and along the long axis of the barrier (Fig. 3). The initial linear velocity V and angular velocity ω are calculated using formulas (4) and (5), respectively, as shown in Table 5.

7 Calculation Result

The impact processes of the different conditions are approximately equal. Figures 6a–e compare the overall response of the barrier throughout the impact process for $\psi = 0$ and $\psi = 0.4$. At 0.1 s, contact between the block and wire ring net is established; at 0.5 s, the steel post deflection displacement is at its

Table 3 Slope angle corresponding to μ

α (°)	μ	α (°)	μ	α (°)	μ
79	0.85	83	0.89	87	0.95
80	0.86	84	0.905	88	0.965
81	0.87	85	0.92	89	0.98
82	0.88	86	0.935	90	1.00

Table 4 Kinetic energy corresponding to various values of ψ

ψ	μ	Slope angle (°)	E_{va} (kJ)	E_{ra} (kJ)
0	1	90	1000	0
0.1	0.95	87	909	91
0.2	0.91	84.5	833	167
0.3	0.88	82	769	231
0.4	0.85	79	714	286

Table 5 Initial velocity of the block

	ψ	V (m/s)	ω (rad/s)
1	0	17.99	0.00
2	0.1	17.15	10.08
3	0.2	16.42	13.64
4	0.3	15.78	16.06
5	0.4	15.20	17.87

maximum; at 1.5 s, the block reaches the maximum displacement after a small rebound; and at 2.0 s, the calculation is terminated.

7.1 Block Displacement

Compared with the non-rotating condition ($\psi = 0$), after applying the rotational kinetic energy, the block has a significant external rolling trend, and the upper support rope deformation increases, as shown in Fig. 6e, f.

H_f is defined as the horizontal distance between the anchorage point of the anchor rope and the block centroid; H_v is the vertical distance between the lower

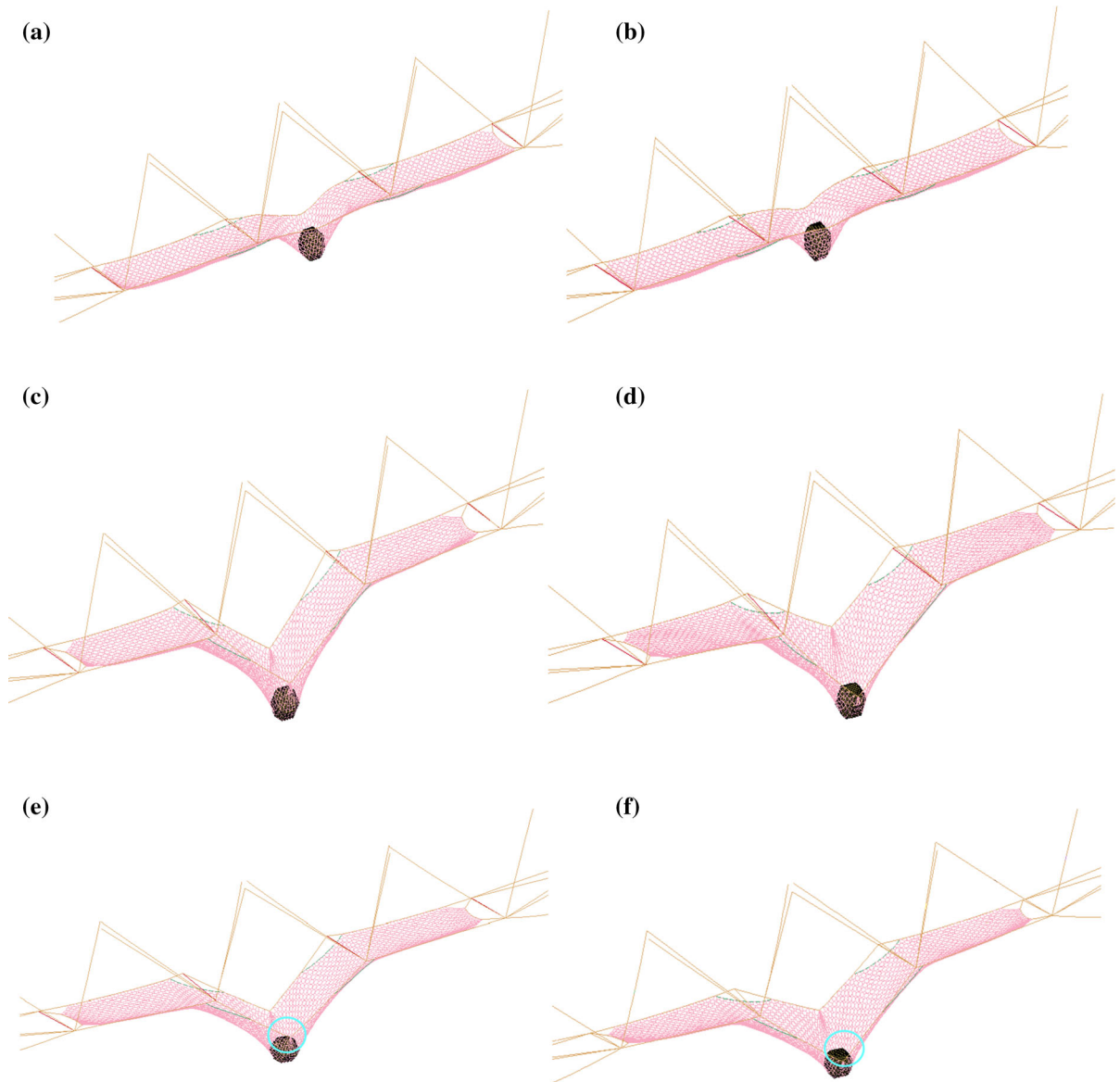


Fig. 6 Dynamic response of the barrier. **a** $\psi = 0, 0.1$ s, **b** $\psi = 0.4, 0.1$ s, **c** $\psi = 0, 0.5$ s, **d** $\psi = 0.4, 0.5$ s, **e** $\psi = 0, 2.0$ s and **f** $\psi = 0.4, 2.0$ s

surface of the block and the upper support rope (Fig. 7). H_{max} is the maximum block displacement.

$\psi = 0.1$ is set as a demarcation point. After the increase and decrease, the basic model remains unchanged, and the maximum vertical displacement of the block is determined. H_{max} decreases because the impact force decreases. These results are shown in Table 6.

7.2 Steel Post Displacement

In an actual project, the free end of the steel post is free to rotate in the vertical plane. The results show that the displacement of the free end of the side post is considerably smaller than that of the middle steel post. At 0.5 s, the midspan steel post free end almost reaches its peak displacement in all three directions (Fig. 8). As ψ increases, the maximum displacement

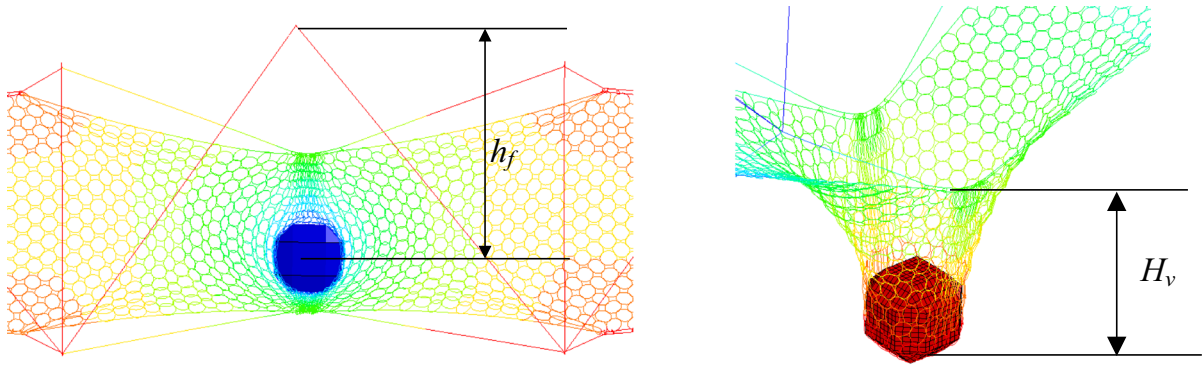


Fig. 7 Relative displacement of H_f and H_v

Table 6 Maximum displacement for different ψ

ψ	H_f (m)	H_v (m)	H_{max} (m)
0	2.43	2.17	6.28
0.1	2.71	1.44	6.22
0.2	2.76	1.45	6.08
0.3	2.77	1.47	5.96
0.4	2.77	1.47	5.85

of the free end of the steel post initially increases and then decreases; the maximum displacement usually occurs when $\psi = 0.2$.

7.3 Impact Force

From 0 to 0.1 s during the block and wire ring net contact, the impact force increases slowly due to the

initial stiffness. From 0.25 to 0.75 s, the block and wire ring net move together and the impact force gradually increases to its peak (Fig. 9). At 0.75 s, the impact force begins to rebound slightly. Then, maximum impact force occurs, which corresponds to the ψ value, as shown in Fig. 10. As the ψ value increases, the impact force decreases. When $\psi = 0$, the maximum impact force is 563.4 kN. When $\psi = 0.4$, the maximum impact force is reduced to 500.6 kN, yielding a reduction of 11.5% compared to the case of $\psi = 0$.

7.4 Maximum Internal Force of the Net

The interaction between the block and wire ring net causes the internal force of the net to increase. The internal force of the midspan is enhanced significantly, while the force does not change on either side of the

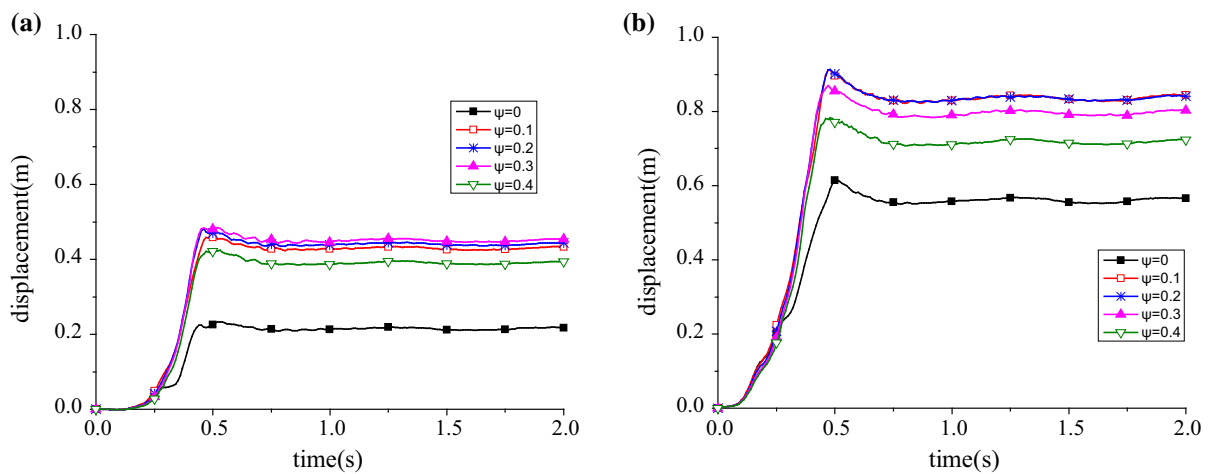


Fig. 8 Displacement of the free end of the middle steel post: **a** X displacement and **b** Z displacement

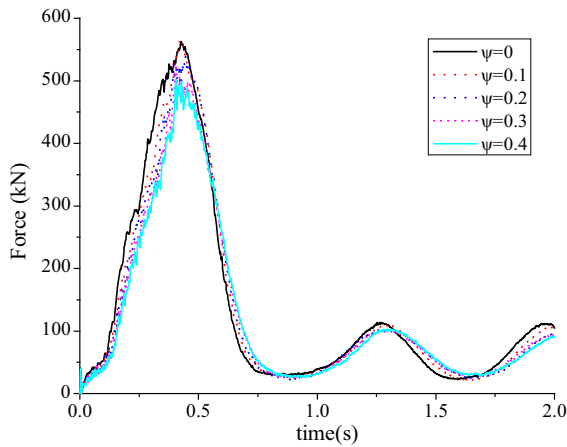


Fig. 9 Time history of the impact force

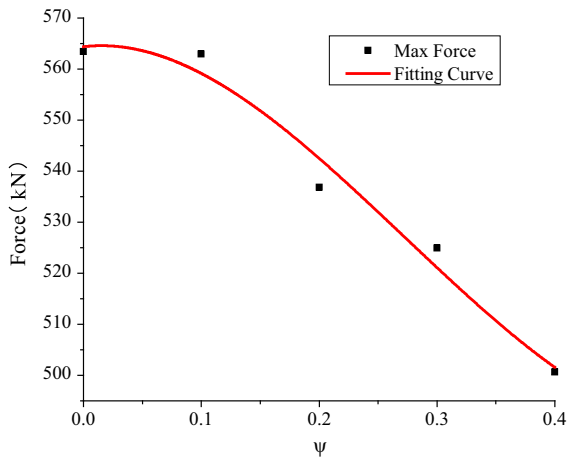


Fig. 10 Distribution of the maximum impact force

net. When $\psi = 0.3$, the internal force of the midspan (NET-2) is the largest. When $\psi = 0.1$, both sides of the net reach their largest internal forces (NET-1, NET-3). The maximum force is 30.57% greater than the case for no rotation.

7.5 von Mises Stress of the Steel Post

When the block is in contact with the wire ring net, the force of the support rope increases because the block rolls out; the force in the rope increases the axial pressure in the steel post and increases the second-order bending moment. As shown in Fig. 11, the stress of the middle post (SP-2 and SP-3) is larger and the stress of the side post (SP-1 and SP-4) is smaller. The

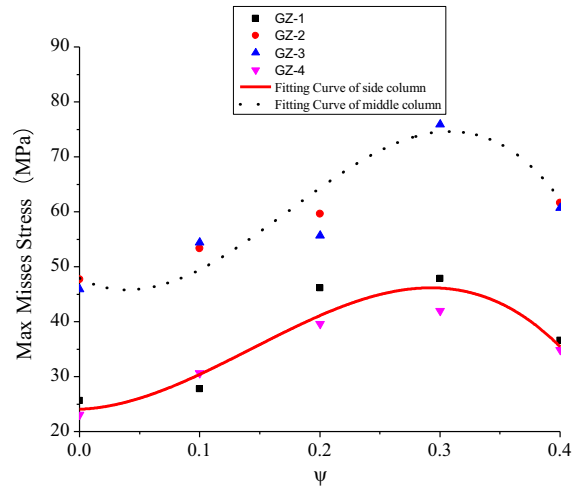


Fig. 11 Maximum von Mises stress of the steel post

steel post stress reaches its stress peak at $\psi = 0.3$ with a maximum increase of 86.85%, and steel post 2 has the greatest stress.

According to Fig. 12, the peak stress value of the posts occurs between 0.25 and 0.75 s. The stress of the middle post increases considerably after the rotation is applied. In addition, as ψ increases, the maximum stress initially increases and then decreases.

7.6 Tensile Force of the Rope

The support rope is directly connected to the net. As the block stops rolling, the force point of the net moves as ψ increases and it shifts to the upper support rope. Therefore, the tension of the upper support rope increases, as shown in Fig. 13. When $\psi = 0.2$, the force reaches a peak value, with a maximum increase of 38.83%. The lower support rope and side support rope exhibit a downward trend, as shown in Fig. 13a, b, respectively, with maximum reductions of 21.98 and 11.88%, respectively.

Under rolling conditions, the force of the middle anchor rope increases greatly and the tensile force of the anchor rope in the side span is smaller. The tensile values of AR-2 and AR-3 reach peak values of 35.71 and 38.69%, respectively, when $\psi = 0.2$. The tensile force of the side anchor rope AR-1 and AR-4 exhibit only slight changes, with a maximum increase of only 14.18%.

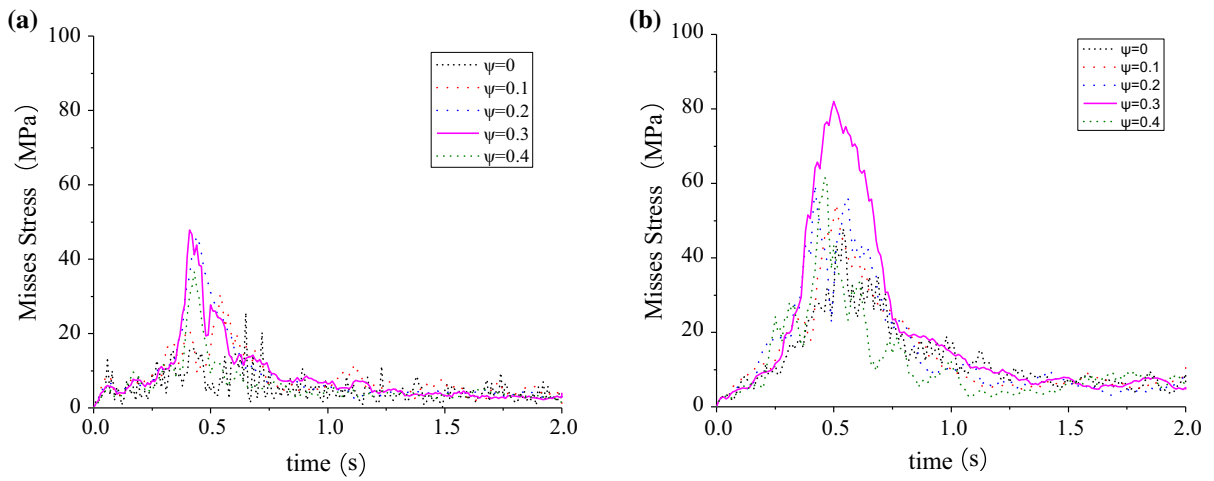


Fig. 12 von Mises stress time history: **a** side post and **b** middle post

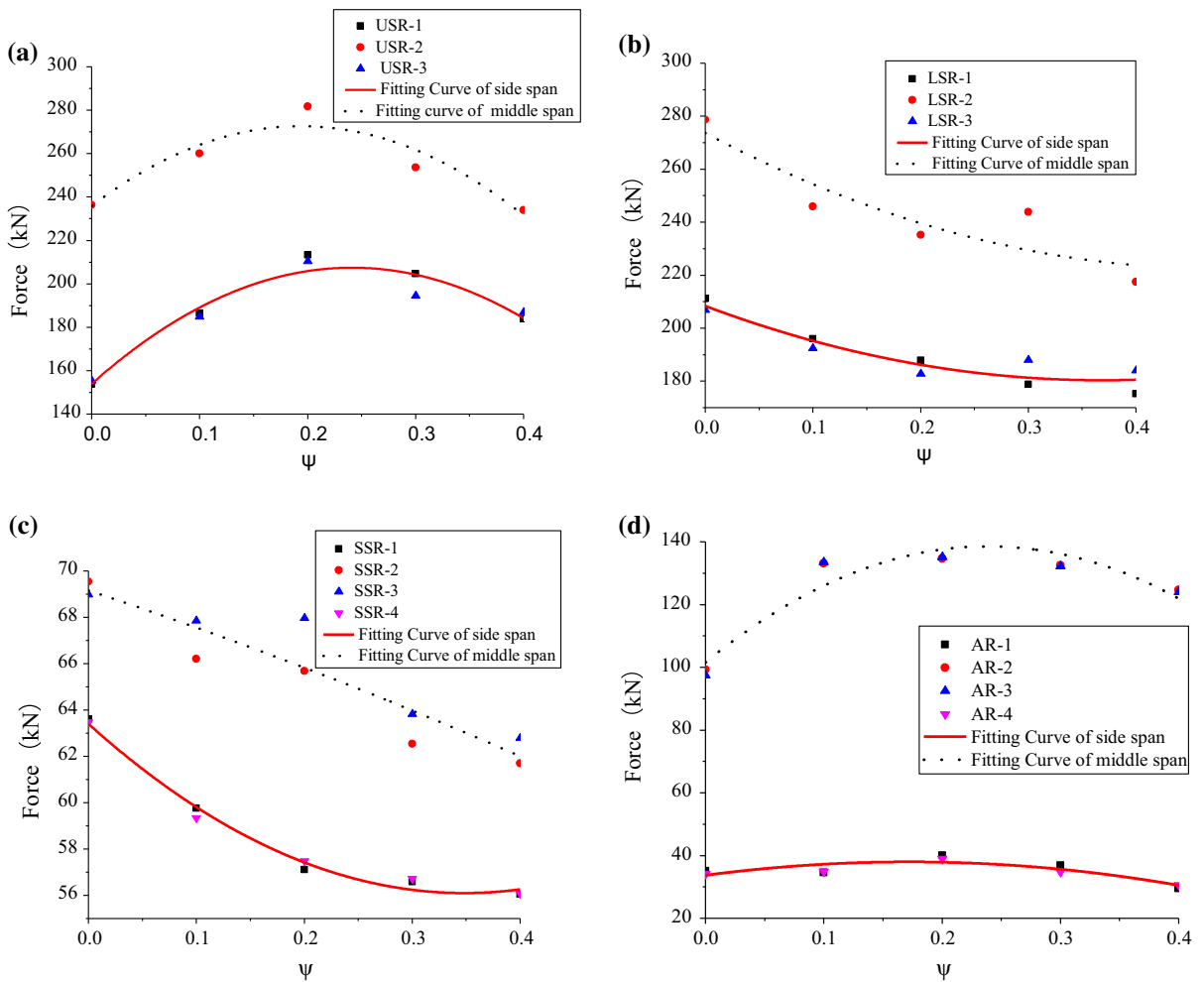


Fig. 13 Maximum tensile force: **a** upper support rope, **b** lower support rope, **c** side support rope, and **d** anchor rope

7.7 System Energy

The rockfall protection barrier is distinguished by its energy distribution. Aside from the net and break rings, the energy dissipation of other components, friction energy consumption and sliding energy dissipation of the system are extremely small. The effect of the break rings in the overall structure is notable because they account for nearly 80% of the total energy displacement. As the ψ value increases, the net and break rings energy consumption exhibit a nearly linear decreasing trend, and the slip and friction energy consumption increase linearly (Fig. 14). Due to rolling, the rockfall and net contact area increases, which increases the consumption of frictional energy. This increase in turn causes the force point to move to the upper support rope and the slip to increase, which is consistent with the energy consumption.

7.8 Correction Factor

To better analyse the relationship between the force of each component and ψ , ψ is used as the independent variable. The internal force or stress extremum of each component is considered to be the dependent variable. The least squares method and polynomial fitting are used to draw trend lines. The fitting coefficient and correlation coefficient R^2 are both shown in formulas (8)–(20), and the fitting curves are shown in Figs. 10, 15 and 11 and 13.

$$F_{impact} = 1105.1\psi^3 - 901.4\psi^2 + 26.7\psi + 564.4 \quad (R^2 = 0.98) \tag{8}$$

$$F_{net-side} = 41788\psi^3 - 29825\psi^2 + 5271.9\psi + 1658.1 \quad (R^2 = 0.57) \tag{9}$$

$$F_{net-middle} = 22738\psi^3 - 23782\psi^2 + 7093\psi + 2194.9 \quad (R^2 = 0.86) \tag{10}$$

$$\sigma_{post-side} = -1671.5\psi^3 + 719.3\psi^2 + 8.2\psi + 24.1 \quad (R^2 = 0.86) \tag{11}$$

$$\sigma_{post-middle} = -2984.1\psi^3 + 1560.9\psi^2 - 111\psi + 47.9 \quad (R^2 = 0.75) \tag{12}$$

$$F_{usr-side} = -921.9\psi^2 + 444.5\psi + 153.9 \quad (R^2 = 0.93) \tag{13}$$

$$F_{usr-middle} = -974\psi^2 + 378.6\psi + 235.8 \quad (R^2 = 0.77) \tag{14}$$

$$F_{lsr-support-side} = 207\psi^2 - 152\psi + 208 \quad (R^2 = 0.87) \tag{15}$$

$$F_{lsr-support-middle} = 228\psi^2 - 216\psi + 274 \quad (R^2 = 0.63) \tag{16}$$

$$F_{ssr-side} = 60.2\psi^2 - 41.9\psi + 63.4 \quad (R^2 = 0.99) \tag{17}$$

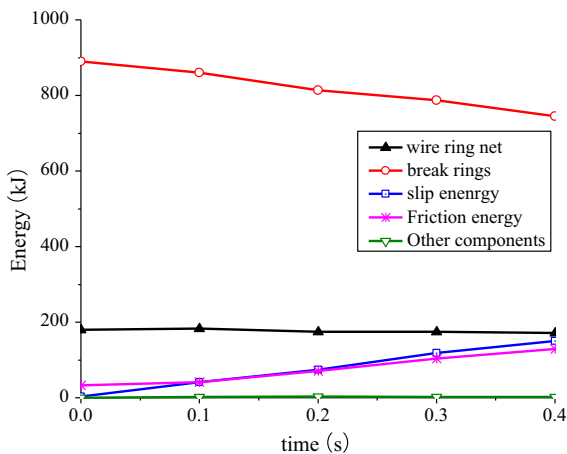


Fig. 14 Energy distribution

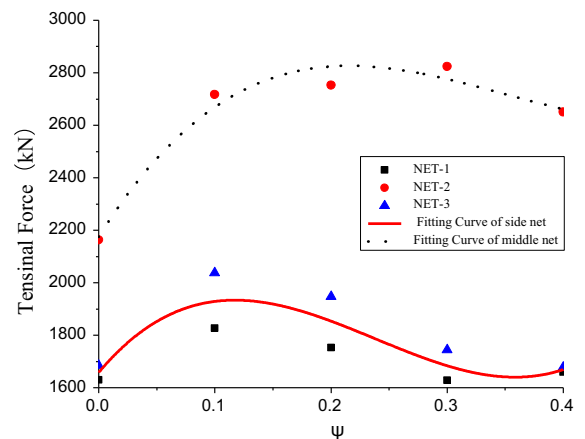


Fig. 15 Maximum internal force of the wire ring net

$$F_{ssr-middle} = -6\psi^2 - 15.5\psi + 69.2 \quad (R^2 = 0.83) \quad (18)$$

$$F_{ar-side} = -144.4\psi^2 + 49.7\psi + 33.7 \quad (R^2 = 0.68) \quad (19)$$

$$F_{ar-middle} = -644.5\psi^2 + 308.7\psi + 101.6 \quad (R^2 = 0.87) \quad (20)$$

To more effectively guide the design, η is defined as a correction factor that considers the rotation effect:

$$\eta = \frac{F_r}{F_{max}} \text{ or } \frac{\sigma_r}{\sigma_{max}} \quad (21)$$

where F_r represents the internal force of the net, the tensile force of the upper support rope, and σ_r represent the stress of the steel post. F_{max} and σ_{max} represent the maximum values of the force and stress, respectively, of the internal components when $\psi = 0$. F_r and σ_r represent the fitting formula to derive the stagnation points ψ_1 and ψ_2 . The maximum internal force of the net, the maximum tension of the upper support rope and anchor rope, and the maximum stress of the steel post are all calculated, and the values are shown in Table 7.

After considering the rotation effect, the largest increase in the steel post stress is 3.76 times the value without rotation. The tensile force in the rope is approximately 1.4, which is considerably larger than the result when $\psi = 0$. Therefore, in the actual design and calculation of the structure, the influence of the rotation effect of the rockfall must be considered and the calculated results must be corrected.

8 Conclusions

Based on the numerical simulations, the following conclusions regarding introducing the ratio ψ of the rotational kinetic energy to the translational kinetic energy are obtained:

1. The rotation effect of the rockfall has a negative impact on the main components of the barrier; the test and design should account for this negative impact.
2. After applying the rotational kinetic energy, the maximum vertical displacement of the rockfall decreases as ψ increases. There is a deviation from the rockfall trend, which results in increased deformation of the upper support rope. As ψ increases, the maximum displacement of the free end of the steel post initially increases and then decreases; the maximum value occurs when $\psi = 0.2$.
3. The tensile forces of the upper support rope and the anchor rope reach their peak values when $\psi = 0.2$, with maximum increases of 38.83 and 38.69%, respectively. The internal force of the net and the von Mises stress of the steel post reach their peak values when $\psi = 0.3$, with maximum increases of 30.57 and 86.85%, respectively.
4. Combining the fitting formula between the force extremum and the ψ of each component provides a reference for further analysis of the barrier structure response to the rotational kinetic energy response. Considering the rotation effect, the internal force correction coefficient of the steel

Table 7 Correction coefficients η

Member	ψ_1	ψ_2	F_r (σ_r)	F_{max} (σ_{max})	η
<i>Net</i>					
Side span	0.359	0.117	1933.6	1657.4	1.17
Middle span	0.481	0.216	2846.6	2162.9	1.32
<i>Steel post</i>					
Side span	0.000	0.290	46.2	25.6	1.80
Middle span	0.004	0.310	74.6	47.7	1.56
<i>Upper support rope</i>					
Side span	0.241	–	207.5	154.6	1.34
Middle span	0.194	–	272.6	236.3	1.15
<i>Anchor rope</i>					
Side span	0.172	–	38.0	34.7	1.10
Middle span	0.239	–	138.6	98.4	1.41

post reached 1.8. Therefore, tests and designs should consider the influence of the rotation effect to ensure adequate safety margins.

Acknowledgements The work of this study was supported by the National Natural Science Foundation of China (Grant Nos. 51408498, 51678504), the foundation of the State Key Laboratory of Geohazard Prevention and Geoenvironment Protection (Grant No. SKLGP2016K013) and the Fundamental Research Funds for the Central Universities (Grant No. 2682017CX006).

References

- Buzzi O, Spadari M, Giacomini A et al (2013) Experimental testing of rockfall barriers designed for the low range of impact energy. *Rock Mech Rock Eng* 46(4):701–712
- EOTA (2012) Guideline for European technical approval of falling rock protection kits (ETAG 027) (February, Brussels)
- Gentilini C, Govoni L, Miranda SD et al (2012) Three-dimensional numerical modelling of falling rock protection barriers. *Comput Geotech* 44(44):58–72
- Gentilini C, Gottardi G, Govoni L et al (2013) Design of falling rock protection barriers using numerical models. *Eng Struct* 50(3):96–106
- Glover J, Volkwein A, Dufour F, Denk M, Roth A (2010) Rockfall attenuator and hybrid drape systems-design and testing considerations. In: Proceedings of the AGS, Tunisia
- Gottardi G, Govoni L (2010) Full-scale modelling of falling rock protection barriers. *Rock Mech Rock Eng* 43(3):261–274
- Hu H (1989) Collapse and rockfall. China Railway Publishing House, Beijing (**in Chinese**)
- Koo RCH, Kwan JSH, Lam C et al (2017) Dynamic response of flexible rockfall barriers under different loading geometries. *Landslides* 14:905–916
- Moon T, Oh J, Mun B (2014) Practical design of rockfall catchfence at urban area from a numerical analysis approach. *Eng Geol* 172(5):41–56
- National Council (2009) Colorado's full-scale field testing of rockfall attenuator systems. *Transportation Research E-Circular*
- Spadari M et al (2013) Statistical evaluation of rockfall energy ranges for different geological settings of New South Wales, Australia. *Eng Geol* 158(8):57–65
- Suits LD, Sheahan TC, Castro-Fresno D et al (2009) Design and evaluation of two laboratory tests for the nets of a flexible anchored slope stabilization system. *ASTM Geotech Test J* 32(4):315–324
- Volkwein A (2005) Numerical simulation of flexible rockfall protection systems. In: Proceedings of the international conference on computing in civil engineering, July 12–15, 2005, Cancun, Mexico
- Zhao S, Zhixiang Y, Wei T et al (2013) Test study of force mechanism and numerical calculation of safety netting system. *China Civ Eng J* 46(5):122–128 (**In Chinese**)